ACS OMEGA

Article

Cite This: ACS Omega 2019, 4, 11380−11387

http://pubs.acs.org/journal/acsodf

Planar Heterojunction Solar Cell Employing a Single-Source Precursor Solution-Processed Sb_2S_3 Thin Film as the Light Absorber

Muthusamy Tamilselvan,[†] Archana Byregowda,[‡] Ching-Yuan Su,[§] Chung-Jen Tseng,[∥] and Aninda J. Bhattacharyya*[,†]

[†]Solid State and Structural Chemistry Unit, Indian Institute of Science, Bengaluru 560012, India

[‡]Jawaharlal Nehru Technological University, Department of Chemistry, Ananthpur, Hyderabad 500085, India

[§]Graduate Institute of Energy Engineering and [∥]Department of Mechanical Engineering/Institute of Energy Engineering, National Central University, Taoyuan City 32001, Taiwan

Supporting Information

ABSTRACT: We discuss here a solution-processed thin film of antimony trisulphide (Sb_2S_3; band gap ≈ 1.7 eV; electronic configuration: ns^2np^0) for applications in planar heterojunction (PHJ) solar cells. An alternative solution processing method involving a single-metal organic precursor, viz., metal−butyldithiocarbamic acid complex, is used to grow the thin films of Sb_2S_3. Because of excess sulphide in the metal complex, the formation of any oxide is nearly retarded. Sb_2S_3 additionally displays structural anisotropy with a ribbon-like structure along the [001] direction. These ribbon-like structures, if optimally oriented with respect to the electron transport layer (ETL)/glass substrate, can be beneficial for light-harvesting and charge-transport properties. A PHJ solar cell is fabricated comprising Sb_2S_3 as the light absorber and CdS as an ETL coated on to FTO. With varying film sintering temperature and thickness, the typical ribbon-like structures predominantly with planes *hkl*: $l = 0$ stacked horizontally along with respect to CdS/FTO are obtained. The morphology of the films is observed to be a function of the sintering temperature, with higher sintering temperatures yielding compact and smooth films with large-sized grains. Maximum photon to electricity efficiency of 2.38 is obtained for PHJ solar cells comprising 480 nm thick films of Sb_2S_3 sintered at 350 °C having a grain size of few micrometers (>5 μm). The study convincingly shows that improper grain orientation, which may lead to nonoptimal alignments of the intrinsic structure with regard to the ETL/glass substrate, is not the sole parameter for determining photovoltaics performance. Other solution-processing parameters can still be suitably chosen to generate films with optimum morphology, leading to high photon to electricity efficiency.

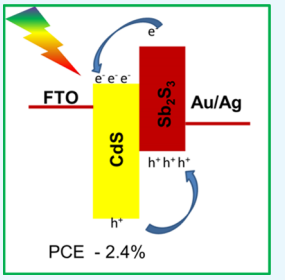

1. INTRODUCTION

Rapid technological advancements in the 21st century has led to a drastic rise in energy demand and consumption. To meet the growing energy demands, harnessing energy from alternative renewable sources has become increasingly important. It has been already forecasted that mankind's entire energy requirements will be met by technologies harnessing energy derived from nonconventional renewable sources. Photovoltaics (PV), which involves direct harness of energy of the sun to electricity, is highly promising as it can provide abundant clean energy at an affordable cost. Diverse materials ranging from crystalline (including nanoparticles) to amorphous systems, small organic molecules to polymers have shown great promise in conversion of the solar photon to electricity.[1−3] Polycrystalline silicon, cadmium telluride (CdTe), copper indium gallium selenide, gallium arsenide (GaAs), and gallium indium phosphide (GaInP) semiconductors are some of the widely studied materials and few of these have made their way in to practical solar cells.[2] However, high processing and fabrication cost as in the case of silicon, poor availability of rare earth elements such as indium and gallium, and severity of environmental implication (e.g., toxicity of Cd) pose a formidable hurdle toward large-scale deployment of solar cells.[4,5] Therefore, research has focussed on seeking for alternative light-harvesting materials. In this context, low-cost semiconductors like copper zinc tin sulfide, cuprous oxide (Cu_2O), copper tin sulfide (Cu_2SnS_3), iron sulfide (FeS_2), zinc phosphide (Zn_3P_2), and cuprous sulfide (Cu_2S) are promising light absorbers.[6−10] However, undesirable implications due to copper defects, multiple phase crystal structure, and low optical band gap are additional drawbacks and pose formidable challenges toward maximization.[11−13] Recently, organic−inorganic hybrid methyl ammonium lead halide ($MAPbX_3$) semiconductors have attracted widespread attention because of achievement of record breaking efficiency of photon to electricity conversion efficiencies.[14,15] However, commercial applications of organic and inorganic hybrid materials are presently limited because of drawbacks, for example, chemical instability, phase transitions, and chemical compositions comprising toxic elements.

To circumvent all of the above detrimental features, sustained efforts are necessary to develop stable ecofriendly

Received: May 1, 2019
Accepted: June 10, 2019
Published: July 1, 2019

DOI: 10.1021/acsomega.9b01245
ACS Omega 2019, 4, 11380−11387

and low-cost alternative light absorbers. Binary metal sulphide semiconductor, antimony(III) sulphide (Sb_2S_3), is an attractive light absorber material because of its high chemical stability and is composed of earth abundant elements. Moreover, antimony sulphide is relatively less toxic compared to extensively studied Cd- and Pb-based sulphides in the field of PV.[5,16] Antimony sulphide has an optimal indirect optical band gap of 1.7 eV and possesses high optical coefficient ($\approx 10^5$ cm^{-1}). This makes it an ideal solar photon harvesting material.[17,18] Reference 19 highlights that the ns^2np^0 class of semiconductors also posses large dielectric constant, small charge carrier effective mass, antibonding states placed under the valence band states, and high defect tolerance, which are expectedly going to enhance the optoelectronic performances. We expect that the antimony sulphide discussed here will also possess similar beneficial properties. Unlike other conventional solar absorber materials which possess the cubic crystal structure, orthorhombic Sb_2S_3 is known to form infinite $(Sb_4S_6)_n$ ribbon-like structures along the *c*-axis and very low dangling bonds at the surfaces perpendicular to (001) plane.[20] This exhibits the highly anisotropic charge transport properties along the ribbon structure. The anisotropic nature of this material provides unique challenges for fabrication of devices, and the performance is inevitably linked to the orientation of the planes.[21] This is reflected in the solar photon to electricity conversion efficiencies where Sb_2S_3 has been employed as a light absorber. In recent times, solar photon to electricity conversion efficiency of 6.35 and 5% have been reported for mesoscopic solar cells (with organic hole conductor) and Schottky-type planar heterojunction (PHJ) solar cells, respectively.[21,22] Though mesoscopic cells show high efficiency compared to the PHJ type, it has an additional hole conductor. Organic-based molecular semiconductors are generally, unstable under ambient conditions and cost intensive. Therefore, development of PHJ with a high photon to electricity conversion efficiency is necessary to develop sustainable technologies in the PV industry for long-time applications.

Rapid thermal annealing, thermal evaporation, and atomic layer deposition are some of the processing techniques which have been used to fabricate the Sb_2S_3 PHJ solar cell having the efficiency 3.5, 1.27, and 5.77%, respectively.[22−25] However, these methods involve dedicated fabrication facilities with vacuum and high temperature to form highly crystalline large-sized grains. Chemical bath deposition is a low-temperature process. However, with this process, there is always a possibility for the formation of Sb_2O_3 along with Sb_2S_3 thin films with small grains.[26,27]

We demonstrate an alternative metal−organic precursor to fabricate both CdS (electron transport layer ETL) and Sb_2S_3 (light absorber material) for PHJ solar cells. Compact and uniform layers of ETL and light absorber have been achieved using a low-cost metal−organic precursor (metal−butyldithiocarbamate) and spin-coating technique at different sintering temperatures (275−350 °C). Because of the structural anisotropy in Sb_2S_3, which may have a detrimental effect on electronic transport, the processing parameters influencing the crystallinity and thickness are studied in detail to optimize the PV performance.

2. RESULTS AND DISCUSSION

The reaction between butylamine and carbon disulphide in ethanol/toluene results in the formation of the butyldithiocarbamic acid (BDCA). BDCA efficiently solubilizes most of the added metal oxide by forming a metal−butyldithiocarbamate complex.[28−30] The stable metal carbamate complex is then cast on the CdS/FTO substrate and heated at moderate temperature to convert it to the metal sulphide in amorphous form. Further sintering at high temperatures leads to pure crystalline (thin film) metal sulphides. The thickness of the film is varied by varying the spin rate, and it will be discussed in later section. The crystallinity and orientation of the Sb_2S_3 thin films are studied using X-ray diffraction (XRD). Figure 1a shows the XRD pattern of Sb_2S_3 films (sintered at 350 °C) on CdS-coated FTO glass along with the powder Sb_2S_3 sample. Based on the Scherrer formula, the crystallite size of Sb_2S_3 thin film at 350 °C is approximately 56 nm. The XRD pattern of the powder Sb_2S_3 is in good agreement with the standard pattern as per JCPDS no. 00-042-1393 (space group: *Pbnm*; *a* = 11.2390 Å; *b* = 11.3130 Å; *c* = 3.8411 Å and $\alpha = \beta = \gamma = 90°$). This strongly suggests that the powder form of Sb_2S_3 prepared using the adopted method is in single phase with high crystallinity. The XRD pattern of the thin film of Sb_2S_3/CdS/FTO sample is observed to be different from that of the powder sample. In general, the intensity of a few planes is lower for the thin film sample compared to the powder sample. This is attributed to the oriented growth on the substrate (vide infra). Bulk crystals of antimony chalcogenides (sulphide, selenide) consist of strongly (chemically) bonded 1-D ribbons of $[Sb_4S_6]_n$ units along the [001] direction as shown in Figure 1b−d. However, in the [100] and [010] directions, the ribbon structures are held together by weak van der Waals forces.[31] The intrinsic morphology of Sb_2S_3 in the thin film changes significantly by varying the sintering temperature (250−400, 280−350, 500−550 °C).[22,32,33] In some cases, the orientation of the thin film depends on the nature of the substrate. For

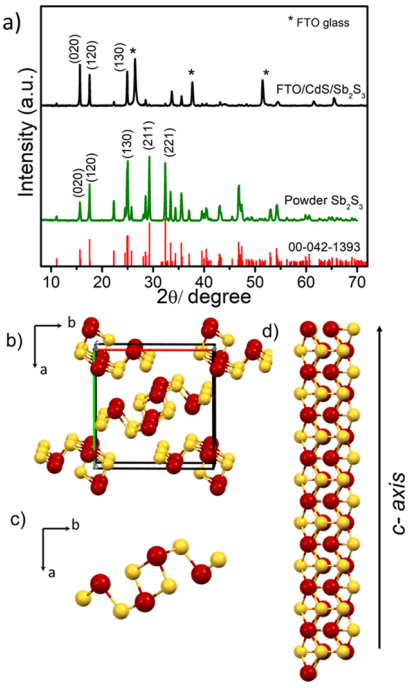

Figure 1. (a) XRD pattern of Sb_2S_3 in powder form, thin film of Sb_2S_3 on CdS/FTO glass. The pattern in red shows the reference pattern (JCPDS no. 00-042-1393). (b) Unit cell of Sb_2S_3 while viewing along the *c*-axis, (c) single unit of $[Sb_4S_6]_n$ and (d) the ribbon structure of Sb_2S_3 viewing along the *a*-axis (red sphere: Sb, yellow sphere: S).

DOI: 10.1021/acsomega.9b01245
ACS Omega 2019, 4, 11380−11387

instance, the bare glass and CdS-coated FTO substrates grow preferentially displaying, respectively, (hkl): $l \neq 0$ and (hkl): $l = 0$ planes in the diffraction pattern.[32] From the XRD pattern of the Sb_2S_3 on CdS/FTO substrate (Figure 2a), it is observed that intensity of $(hk0)$ planes (020), (120), (130) is higher in comparison to (hkl) planes (211), (221).

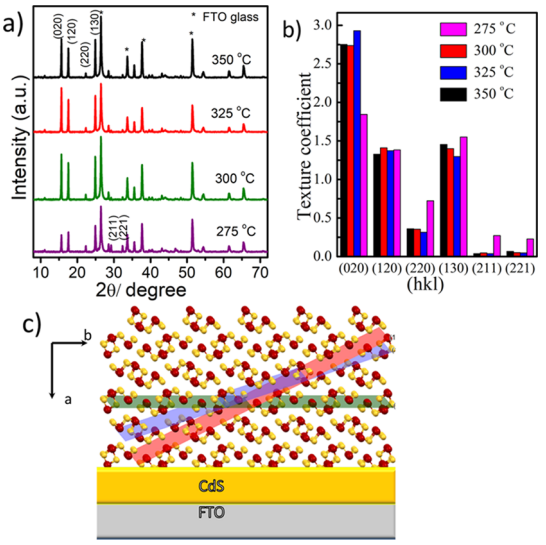

Figure 2. (a) Temperature-dependent powder XRD patterns of Sb_2S_3. (b) Texture coefficient (T_C) of selected diffraction peaks in Sb_2S_3 thin film at different temperatures. (c) Schematic presentation of horizontal packing of $[Sb_4S_6]_n$ ribbon structure on the CdS/FTO substrate while viewing along the c-axis. Rectangle strips represent the planes [green: (020), red: (120), blue: (130)].

For preferential orientation growth, texture coefficient (T_C) of Sb_2S_3 thin film samples at various sintering temperatures are calculated and displayed in Figure 2b by using the following equation: $T_c = n\frac{(I/I_o)}{\sum I/I_o}$, where parameters I, I_o, and n are the measured diffraction peak intensity, diffraction peak intensity of reference pattern, and total number of selected diffraction peaks taken in the calculation. Larger T_C value for particular diffraction peaks indicates the preferred orientation along the particular plane of the thin film. From the texture coefficient (T_C) values, the $(hk0)$ planes were higher than (hkl) planes. This confirms that in general, the $(hk0)$ planes are highly textured in the Sb_2S_3 thin films formed from the metal organic single-source precursors and growth is oriented at $[hk0]$. While increasing the sintering temperature from the 275 to 350 °C, the T_C values remain higher for $(hk0)$ planes than those of the (hkl) planes as shown in Figure 2b. From this, we conclude that the orientation of the thin film growth is not affected by the sintering temperature. Figure 2c depicts the $(hk0)$ plane orientation of Sb_2S_3 thin film on the CdS/FTO glass substrate.

Trap and surface states in the semiconductor are generated by the covalent bond breaking (dangling bond) at the surfaces.[34−37] The 1-D ribbon structure Sb_2S_3 has the advantage that there are no dangling bonds along the $(hk0)$ plane surfaces.[38] Absence of dangling bonds and hence the defects are manifested via high intensity of diffraction peaks from $(hk0)$ crystal planes. This will expectedly lead to lower charge trapping in the optoelectronic devices. In general, the $(hk0)$ oriented growth of antimony chalcogenide semiconductors shows a decrease in photon to electron conversion efficiency because of significant increase in the series resistance.[38] We anticipate here that the optimally thick crystalline Sb_2S_3 films will bypass this problem and expectedly enhance the efficiency in PHJ solar cells. As shown in Figure S1, the T_C values of the Sb_2S_3 films of varying thickness (at constant temperature) also follow the same trend with the (hkl): $l = 0$ planes showing higher value compared to (hkl): $l \neq 0$. Therefore, there is no texture difference observed at the Sb_2S_3 morphology by varying the film thickness. Thus, it is important to note that a highly crystalline film with an optimum thickness is an important parameter for the development of high-efficiency PHJ solar cells. From the observation of the cross-sectional field emission scanning electron microscopy (FESEM) images (Figure S4), the thickness of the Sb_2S_3 layer is found to be 270, 360, 480, and 630 nm for spinning speeds at 5000, 4000, 3000, and 2000 rpm, respectively, at sintering temperature of 350 °C.

Figure 3 shows the optical absorbance spectrum of Sb_2S_3 films of varying thickness grown on the CdS/FTO substrate

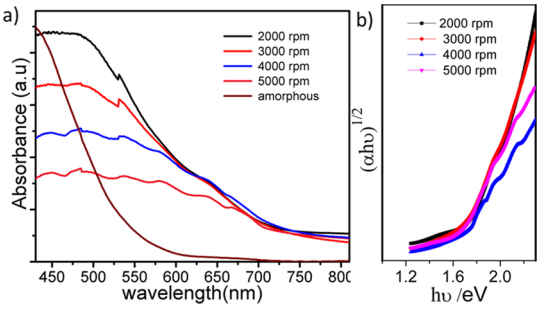

Figure 3. (a) UV−visible light absorbance spectrum of Sb_2S_3 at different spin rates and final sintering temperature of 350 °C. UV−visible spectrum of the films sintered at 200 °C (amorphous) is also shown in the same plot and (b) Tau plots to measure the indirect band gap.

along with the amorphous Sb_2S_3 film formed prior to the sintering process. The CdS (E_g = 2.5 eV) thin film on FTO glass absorbs slightly in the visible light region,[39] compared to other wide band gap metal oxide (e.g., TiO_2, ZnO, SnO_2) ETLs used in optoelectronic devices.[40] Additional absorption of light by CdS along with Sb_2S_3 would be beneficial as this effectively increases the absorption of the visible light. The amorphous Sb_2S_3 on CdS starts to absorb light at around 570 nm. Once the film is sintered above the 275 °C, Sb_2S_3 becomes crystalline in nature and the visible light absorption region increases and extends up to the IR region and exhibits an indirect band gap of 1.7 eV (estimated using Tauc plot, Figure 3b). From Figure 3a we can conclude that when the thickness of the light absorber Sb_2S_3 increases by decreasing spinning speed from 5000 to 2000 rpm, the optical absorption range in the visible wavelength region gradually increases. There are no notable changes in the absorption spectrum of Sb_2S_3 because of different sintering temperature processes.

Atomic force microscopy (AFM) and FESEM are used to characterize the roughness and morphology of the Sb_2S_3 layer on the CdS/FTO glass surface. In Figure S2, FESEM images of CdS-coated FTO glass show the uniform coverage of CdS (layer thickness ≈ 120 nm) on the rough FTO surface. The root mean square (rms) roughness of CdS on FTO glass is around 5.15 nm, which has a lower rms value compared to the bare FTO glass of 29.2 nm (Figure S3). Generally, the

DOI: 10.1021/acsomega.9b01245
ACS Omega 2019, 4, 11380−11387

morphology of the absorber layer in PHJ depends on the sintering temperature and nature of the substrate used in the devices. In this study, growth of Sb_2S_3 layers at various temperatures has been done by keeping the CdS layer on FTO constant. At 4000 rpm, the deposited Sb_2S_3 on CdS/FTO is annealed for a few minutes at 200 °C followed by sintering at various temperature (275 to 350) °C for 15 min. The rms value of Sb_2S_3 on CdS/FTO is around 27 nm for the 275 °C sintered sample, as shown in the Figure 4e–h. At 300 °C, the roughness decreased to 18 nm. With further increase in the sintering temperature, the roughness decreased to 11 nm (at 325 °C) and 8 nm at 350 °C along with gradual increase in the size of grains (Figure 4e–h).

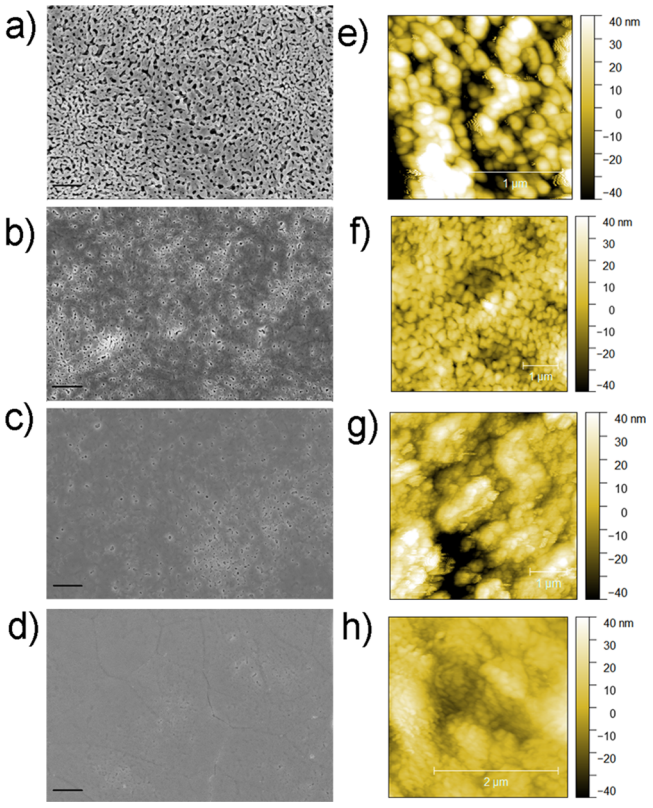

Figure 4. SEM images of Sb_2S_3 on CdS/FTO glass substrate at various annealing temperatures: (a) 275, (b) 300, (c) 325, and (d) 350 °C. All SEM images are having a scale of 1 μm. AFM images of Sb_2S_3 on CdS/FTO glass substrate at various annealing temperatures: (e) 275, (f) 300, (g) 325, and (h) 350 °C.

At 275 °C, the particles in the Sb_2S_3 film are agglomerated. The agglomerates are separated by large amounts of voids. With the increase in temperature, the particles start to grow in size, leading to the elimination of the voids. This is observed in the SEM images of Sb_2S_3 on CdS/FTO shown in Figure 4a–d. At 300 °C, the calculated average crystal size is nearly 54 nm as obtained by Scherrer equation and agglomerated grain size is >2 μm with some remnant voids, as observed from the FESEM. At 350 °C sintering temperature, the film shows a glassy texture with an average agglomerate grain size larger than 5 μm with nearly no visible voids on the surface. This ensures that the roughness at the surface is low and this will decrease the short circuit contact between the CdS ETL and gold counter electrode. The larger grain size with high crystallinity will enhance the recombination resistance, leading to better PV performances.[41] The elemental ratio between S and Sb are obtained using EDS measurements, and the values are shown in the Table S1. No drastic changes are observed in the roughness of Sb_2S_3 films of varying thicknesses (at constant sintering temperature).

Because of multiple valence states present in the Sb-based compounds, it is necessary to examine using X-ray photoelectron spectroscopy (XPS) the oxidation states of the various elements constituting Sb_2S_3. The high-resolution core spectrum of the individual elements is fitted with Lorentzian to estimate the binding energy and oxidation states of Sb and S as shown in the Figure 5a,b.

The binding energy of Sb^{+3} oxidation state consists of two main peaks because of spin orbital coupling in the Sb 3d orbitals.[42] In general, the surface adsorbed oxygen 1s peak at around 530 eV, which overlaps with the Sb $3d_{5/2}$ peak in the range 529–530 eV.[21,42−44] Therefore, Sb $3d_{3/2}$ is only considered for the analysis of the oxidation state of Sb. From the Figure 5a, 538.8 eV pertains to the Sb trivalent state. The Sb–O peak at around 540 eV is observed to be insignificant. Figure 5b shows the core spectrum of S. The $2p_{3/2}$ and $2p_{1/2}$ stated differently is 1.2 eV which confirms the minus two oxidation states present in the Sb_2S_3 layer. No extra peak is observed at around 168 eV, which refers to the S in the oxidized form. For Sb_2S_3 prepared using other solution based protocols,[21] additional sulfurization processes are required to remove oxide layers from the Sb_2S_3 layer. However, in the case of the present metal organic precursor protocol, a nearly oxide-free Sb_2S_3 layer is formed without the necessity of any postsintering processes. This is primarily due to the in situ formation of the BDCA complex in the solution which is rich in the sulphide group hindering the formation of the oxide layer.

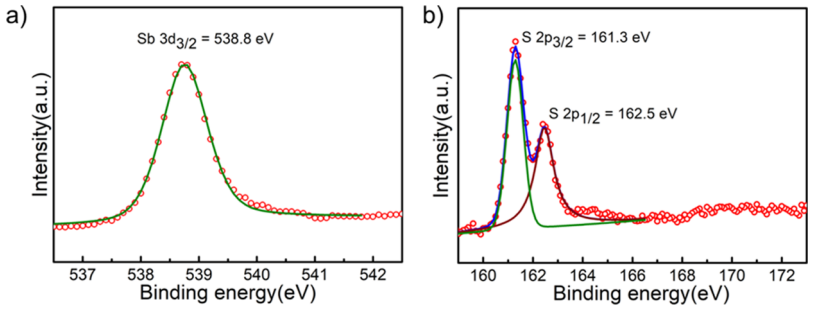

Figure 5. High-resolution core level XPS of Sb $3d_{3/2}$ (a), S 2p (b). Experimental data are shown in red circle, and solid lines represent the fitted values.

DOI: 10.1021/acsomega.9b01245
ACS Omega 2019, 4, 11380−11387

In general, specific device parameters are affected because of elemental loss, microstructural changes, crystal phase, and orientation of growth of the light absorber. The characteristic current density versus voltage behavior of the solar cells under 100 mW cm^{-2} illumination is shown in Figure 6. The specific

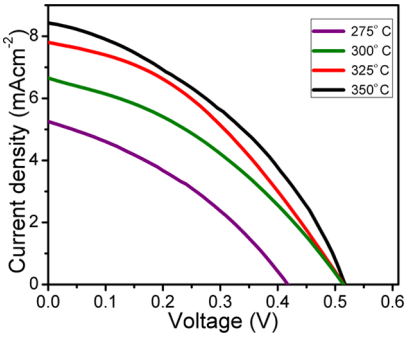

Figure 6. Current density versus voltage curve of the best performance Sb_2S_3/CdS PHJ solar cell fabricated at various sintering temperatures.

Table 1. PV Parameters of Solar Cells Fabricated with Sb_2S_3 Films Sintered at Various Temperatures

sintering temperature (°C)	V_{OC} (V)	J_{SC} (mA cm^{-2})	FF	PCE (%)	R_{Sh} (Ω cm^2)	R_S (Ω cm^2)
275	0.42	5.23	0.35	0.78	162.8	41.7
300	0.52	6.68	0.37	1.28	195.4	41.5
325	0.52	7.40	0.39	1.50	197.2	30.8
350	0.52	8.44	0.38	1.70	233.0	34.3

parameters of the devices are summarized in Table 1. The power conversion efficiency (PCE) of Sb_2S_3 PHJ incorporated with ETL (CdS) sintered at 275, 300, 325, and 350 °C temperatures is obtained as 0.78, 1.28, 1.50, and 1.70% respectively.

When the sintering temperature increased from 275 to 300 °C, the corresponding open circuit voltage (V_{OC}) increased from 0.42 to 0.52 V, and it reached a stable value of 0.52 V at 325 and 350 °C. As discussed earlier, the change in sintering temperature of Sb_2S_3 affects the microstructure with the crystal structure remaining constant. The lower value of V_{OC} for the device having Sb_2S_3 sintered at 275 °C compared to the other devices is attributed to the large amounts of voids present in the Sb_2S_3 light absorber layer which leads to pin hole formation. High degree of roughness (rms = 27 nm estimated from AFM) and pin hole formation in Sb_2S_3 materials leads to considerable amount of recombination at the CdS buffer layer interface. At elevated temperatures (325 and 350 °C), the V_{OC} becomes constant because of the lower roughness and larger grain size. On the other hand, the J_{SC} value increased from 5.24 at 275 °C to 6.68, 7.40, 8.44 mA cm^{-2} for 275, 300, 325, and 350 °C, respectively. This can probably be attributed to the reduction in the void volume fraction with increase in temperature. The grains increase in size effectively, leading to percolative charge transport.

The increase in temperature also leads to dense packing of the layer along with lower rms values. Though the obtained crystal orientation in the films may not present the best situation for electron transport from the light absorber to the CdS ETL (and hole transport to the metal contact), the well-developed grains along with lower roughness of the film still enhance the efficiency of the PHJ solar cells. The energy is generally dissipated via the two resistance parameters viz. series (R_S) and shunt resistance (R_{Sh}). For ideal rectification, the shunt series should be maximum and series resistance should be minimum in value.[45−47] Based on the linear approximation method,[48] the two resistances are calculated from respective device $I-V$ plots as shown in Table 1. The solar cell with PCE 1.70% shows a high shunt resistance of 233 Ω cm^2. With the increasing annealing temperatures, the R_{Sh} increases because of improved film microstructure and high packing density. This decreases the recombination of the photogenerated charge carriers at the CdS interface. With regard to R_S, the higher the sintering temperature, the lower is the R_S value. The device fabricated at 275 °C recorded the highest value (≈41.7 S cm^2); the lowest value is obtained at 325 °C (≈30.8 S cm^{-2}). Better connectivity between the grains results in decrease in the R_S value.[49,50] The R_S increased from 30.8 S cm^2 at 325 °C to 34.3 S cm^2 at 350 °C. This is attributed to large grains obtained at 350 °C as observed from SEM. We propose that because of optimum roughness of the Sb_2S_3 film at 325 °C, the gold layer fused better with the light absorber, thus forming a better contact with the former. The better contact with Sb_2S_3 leads to lower R_S values at 325 °C. The Sb_2S_3 surface is smooth (low rms value) for the films sintered at 350 °C. This leads to some degree of physical mismatch of the gold with the Sb_2S_3 film sintered at 350 °C, thus leading to the higher contact resistance. Based on the above discussion, we can easily conclude that the 350 °C is optimum temperature for high efficient device fabrication, and the average PV device parameters are obtained at 350 °C and displayed in Table S2.

The morphology and optical density of light absorber materials play an important role in the performance of PHJ solar cell.[51−53] In this context, the performance of PHJ solar cells with the Sb_2S_3 film sintered at 350 °C and with varying thickness (obtained via varying the spinning speed) are studied. The current density versus voltage plots are shown in Figure 7. The best efficiency is obtained for the device with

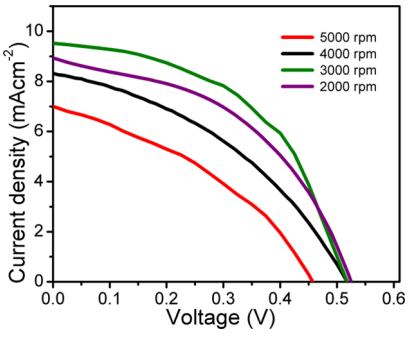

Figure 7. Current density vs voltage curve of the best performance Sb_2S_3/CdS PHJ solar cells fabricated at varying spin rates [5000 rpm: 270 nm, 4000 rpm: 360 nm, 3000 rpm: 480 nm, and 2000 rpm: 630 nm].

Sb_2S_3 thickness of around 480 nm, exhibiting an efficiency of 2.38% (V_{OC} = 520 mV, J_{SC} = 9.52 mA/cm^2, FF = 48%), and the average device parameters (480 nm thickness device) are shown Table S2. The optical absorbance density, pin hole formation, and charge carrier transport is strongly influenced by the thickness of the light absorber.[54] The V_{OC} value shows a

DOI: 10.1021/acsomega.9b01245
ACS Omega 2019, 4, 11380−11387

Table 2. PV Parameters of the Solar Cells Assembled with the Sb_2S_3 Layer of Varying Thickness

spin speed/rpm (thickness/nm)	V_{OC} (V)	J_{SC} (mA cm^{-2})	FF	PCE (%)	R_{Sh} (Ω cm^2)	R_S (Ω cm^2)
5000 (270)	0.460	7.00	0.37	1.20	151.5	30.3
4000 (360)	0.520	8.32	0.39	1.70	204.1	29.4
3000 (480)	0.520	9.52	0.48	2.38	431.6	17.4
2000 (630)	0.520	8.93	0.46	2.15	212.5	18.4

drastic change from the 0.46 to 0.52 V when the thickness increases from 270 to 360 nm. The V_{OC} became nearly constant for the films with thickness of 480 and 630 nm. This can be accounted on the basis of very high possibility of pin hole formation in the PHJ solar cell. When the light absorber material is thinner than the optimized film thickness, higher recombination will take place between the metal contact and ETL.[55] This proposition is supported by the estimated R_{Sh} values, where the thinner film shows a lower shunt resistance (151.5 Ω cm^2) value compared to the thicker film as shown in Table 2. The value of the fill factor for the films of varying thickness shows a trend similar to the V_{OC}.

The J_{SC} values as a function of the film thickness are shown in Table 2. J_{SC} of 8.93 and 9.52 mA cm^{-2} are obtained for 630 and 480 nm, respectively. For the 360 and 260 nm thick films, the J_{SC} values are, respectively, 8.83 and 7.00 mA cm^{-2}. The changes in J_{SC} can be accounted on the basis of the combined effects of optical density and charge carrier transport properties in the Sb_2S_3 layer. The UV−visible light absorbance spectra in Figure 3 support the proposition of the increase in the optical density with increasing thickness of Sb_2S_3 in the devices. This shows that to obtain high optical density and photocurrent, an optimal film thickness, desired diffusion path length, and crystal orientation is absolutely essential. In case of Sb_2S_3, the reported diffusion lengths vary from (290 to 900) nm depending on the light intensity.[56] In this study, film thickness of 480 nm provides the optimal condition for solar cell operation. The effect of film thickness is reflected in the shunt and series resistances as well, as shown in the Table 2. Under the conditions presented here the optimal values of R_S (17.4 Ω cm^2) and R_{SH} (431.6 Ω cm^2) are obtained for the film of thickness 480 nm.

3. CONCLUSION

In summary, we have demonstrated here fabrication of highly crystalline, plane-oriented growth of Sb_2S_3 with controlled morphology starting from a metal−organic precursor. We believe that this work will pave the way for the development of metal sulphides from simple alternative synthesis protocols, such as single-source precursor solution methods to fabricate to PHJ solar cells. By understanding the crystal orientation growth in films obtained from single-source method will provide feasible ways to fabricate other 1-D, 2-D based light absorbers for optoelectronic devices. Our studies convincingly show that sintering temperature and thickness are essential parameters for the final film morphology and crystal orientation which eventually have a significant effect on the solar cell performance.

4. EXPERIMENTAL SECTION

4.1. Preparation of Metal Organic Precursors. Toluene (5 mL) and of 1-butylamine (C_4H_9−NH_2) (3 mL) are taken in a 25 mL glass vial. This is kept inside an ice bath. To the above mixture, 1.5 mL of carbon disulphide (CS_2) solution is added slowly dropwise under gentle stirring. The solution changes from colorless to slightly yellow. This confirms the formation of BDCA. Following this, 1 mmol of antimony(III) oxide is added to the BDCA solution. The mixture is heated at 70 °C for 30 min until the metal oxide is completely dissolved, and the solution turns dark yellow. This solution is further heated to remove unreacted butylamine and CS_2. After removal of unreacted chemicals, the solution becomes highly viscous. The viscosity of this solution typically depends on the added metal oxide concentration. Trace amounts of insoluble metal oxide particles are removed by centrifugation (speed: 8000≈ rpm) and stored in a closed glass vial at room temperature for further use. The CdS precursor solution is also prepared by the protocol as discussed above. Instead of toluene, ethanol is used as the solvent. This resulted in better adhesive films on the fluorine-doped tin oxide glass (Sigma-Aldrich FTO glass—sheet resistance—8 Ω/sq, thickness ≈ 550 nm) substrate compared to when films are cast using toluene.

4.2. Device Fabrication. Before deposition of the CdS ETL, the FTO glass substrate is cleaned with detergent, acetone, and ethanol in a sequential way and dried by blowing N_2 gas. CdS metal organic precursor was added dropwise on to clean FTO glass, which is rotated at a speed of 6000 rpm for 60 s. The CdS/FTO is then baked on the hot plate at around 200 °C for 2 min, followed by sintering at 450 °C under an inert atmosphere for 15 min. The Sb_2S_3 absorber layer of varying thickness is deposited at various spinning speeds viz. at 2000, 3000, 4000, and 5000 rpm. Following this, the sample is annealed at 200 °C for 2 min in a hot plate to remove the organic byproducts. This is followed by sintering the Sb_2S_3 at 275, 300, 325, and 350 °C to convert the amorphous metal sulphide (orange color) to crystalline Sb_2S_3 thin films. Following the sintering process, the film is cooled down to room temperature under the same inert atmosphere to avoid the formation of metal oxide layer on the surface. Finally, the gold counter electrode is deposited by a sputtering unit (JEOL JFC-1100E ion sputtering device) for 15 min at an applied current of 15 mA under vacuum. The active area of each solar cell device is kept nearly constant at approximately 0.04 cm^2 (0.2 × 0.2 cm).

4.3. Characterization. The powder XRD pattern of thin film Sb_2S_3 is recorded using the PANalytical Empyrean X-ray diffractometer; Cu Kα radiation, 1.5418 Å with a nickel filter source operating at 45 kV with 30 mA at a step size and scan speed of 0.026° min^{-1} and 0.033° s^{-1}, respectively. The powder form of the metal sulphide is collected from the thin film. UV−visible spectrum of Sb_2S_3 coated on to the CdS/FTO glass is recorded using solid-state Shimadzu MPC3600 equipped with an integrating sphere for the UV−visible data. Surface morphology and thickness of each layer in the solar cell is examined using scanning electron microscopy (SEM) (Ultra55 FESEM Karl Zeiss) with the help of inlens detector and secondary electron detector facility, respectively. The oxidation states of the elements present in the thin film are obtained using XPS. The XPS data are recorded with AXIS-Ultra using monochromatic Al Kα radiation (225 W, 15 mA,

DOI: 10.1021/acsomega.9b01245
ACS Omega 2019, 4, 11380−11387

15 kV). The Sb_2S_3 sample is scratched out from the FTO glass substrate for the XPS analysis. A Keithley source meter unit (model 2400) is used to perform the current versus voltage ($I-V$) characterization under a simulated 1.5 AM solar irradiation with the power of 100 mW/cm^2. Sciencetech 300 AAA solar simulator (xenon source) is used to generate radiation, and power of the lamp is calibrated using monocrystalline silicon reference cell from NREL. All $I-V$ measurements are carried out in room with controlled atmosphere (humidity > 70% at room temperature).

■ ASSOCIATED CONTENT

Supporting Information

The Supporting Information is available free of charge on the ACS Publications website at DOI: 10.1021/acsomega.9b01245.

XRD patterns of the Sb_2S_3 film of different thicknesses sintered at 350 °C, texture coefficient of the Sb_2S_3 film of different thicknesses sintered at 350 °C, FESEM and AFM images of bare FTO glass and CdS-coated FTO glass, and cross section of FESEM images of deposited Sb_2S_3 on CdS/FTO glass at different spin rates (PDF), elemental analysis of Sb_2S_3 films deposited on the bare glass substrate, average photovoltaic device parameters for optimum sintering temperature and film thickness.

■ AUTHOR INFORMATION

Corresponding Author

*E-mail: anindajb@iisc.ac.in.

ORCID

Ching-Yuan Su: 0000-0001-9295-7587

Aninda J. Bhattacharyya: 0000-0002-0736-0004

Notes

The authors declare no competing financial interest.

■ ACKNOWLEDGMENTS

A.J.B. acknowledges the India−Taiwan Programme of Cooperation in Science and Technology, DST, New Delhi (project reference no. GITA/DST/TWN/P-74/2017), and Amrut Mody Chair Professorship for the financial support and CENSE, IISc., Bengaluru, and SSCU, IISc., Bengaluru, for the infrastructural support.

■ REFERENCES

(1) Kamat, P. V. Meeting the Clean Energy Demand: Nanostructure Architectures for Solar Energy Conversion. *J. Phys. Chem. C* **2007**, *111*, 2834−2860.

(2) Green, M. A.; Hishikawa, Y.; Dunlop, E. D.; Levi, D. H.; Hohl-Ebinger, J.; Ho-Baillie, A. W. Y. Solar Cell Efficiency Tables (Version 51). *Prog. Photovoltaics* **2018**, *26*, 3−12.

(3) Green, M. A.; Pillai, S. Harnessing Plasmonics for Solar Cells. *Nat. Photonics* **2012**, *6*, 130−132.

(4) Ondraczek, J.; Komendantova, N.; Patt, A. WACC the dog: The Effect of Financing Costs on the Levelized Cost of Solar PV power. *Renewable Energy* **2015**, *75*, 888−898.

(5) Peter, L. M. Towards Sustainable Photovoltaics: The Search for New Materials. *Philos. Trans. R. Soc. London, Ser. A* **2011**, *369*, 1840−1856.

(6) Wang, W.; Shen, H.; Wong, L. H.; Su, Z.; Yao, H.; Li, Y. A 4.92% efficiency Cu_2ZnSnS_4 Solar Cell From Nanoparticle Ink and Molecular Solution. *RSC Adv.* **2016**, *6*, 54049−54053.

(7) Minami, T.; Nishi, Y.; Miyata, T. Cu_2O-Based Solar Cells Using Oxide Semiconductors. *J. Semicond.* **2016**, *37*, 014002−014011.

(8) Nakashima, M.; Fujimoto, J.; Yamaguchi, T.; Izaki, M. Cu_2SnS_3 Thin-Film Solar Cells Fabricated by Sulfurization from NaF/Cu/Sn Stacked Precursor. *Appl. Phys. Express* **2015**, *8*, 042303.

(9) Luber, E. J.; Mobarok, M. H.; Buriak, J. M. Solution-Processed Zinc Phosphide (α-Zn_3P_2) Colloidal Semiconducting Nanocrystals for Thin Film Photovoltaic Applications. *ACS Nano* **2013**, *7*, 8136−8146.

(10) Hall, R. B.; Birkmire, R. W.; Phillips, J. E.; Meakin, J. D. Thin-Film Polycrystalline $Cu_2S/Cd_{1-x}Zn_xS$ Solar Cells of 10% Efficiency. *Appl. Phys. Lett.* **1981**, *38*, 925−926.

(11) Zhao, J.-Y.; Zhang, J.-M. Modulating the Band Gap of the FeS_2 by O and Se Doping. *J. Phys. Chem. C* **2017**, *121*, 19334−19340.

(12) Baranowski, L. L.; Zawadzki, P.; Lany, S.; Toberer, E. S.; Zakutayev, A. A Review of Defects and Disorder in Multinary Tetrahedrally Bonded Semiconductors. *Semicond. Sci. Technol.* **2016**, *31*, 123004.

(13) Kumar, M.; Dubey, A.; Adhikari, N.; Venkatesan, S.; Qiao, Q. Strategic Review of Secondary Phases, Defects and Defect-Complexes in Kesterite CZTS−Se Solar Cells. *Energy Environ. Sci.* **2015**, *8*, 3134−3159.

(14) Yang, W. S.; Park, B.-W.; Jung, E. H.; Jeon, N. J.; Kim, Y. C.; Lee, D. U.; Shin, S. S.; Seo, J.; Kim, E. K.; Noh, J. H. Iodide Management in Formamidinium-Lead-Halide−Based Perovskite Layers for Efficient Solar Cells. *Science* **2017**, *356*, 1376−1379.

(15) Sahli, F.; Werner, J.; Kamino, B. A.; Bräuninger, M.; Monnard, R.; Paviet-Salomon, B.; Barraud, L.; Ding, L.; Leon, J. J. D.; Sacchetto, D. Fully Textured Monolithic Perovskite/Silicon Tandem Solar Cells with 25.2% Power Conversion Efficiency. *Nat. Mater.* **2018**, *17*, 820.

(16) Kuhar, K.; Pandey, M.; Thygesen, K. S.; Jacobsen, K. W. High-Throughput Computational Assessment of Previously Synthesized Semiconductors for Photovoltaic and Photoelectrochemical Devices. *ACS Energy Lett.* **2018**, *3*, 436−446.

(17) Kondrotas, R.; Chen, C.; Tang, J. Sb_2S_3 Solar Cells. *Joule* **2018**, *2*, 857.

(18) Zeng, K.; Xue, D.-J.; Tang, J. Antimony Selenide Thin-Film Solar Cells. *Semicond. Sci. Technol.* **2016**, *31*, 063001.

(19) Ganose, A. M.; Savory, C. N.; Scanlon, D. O. Beyond Methylammonium Lead Iodide: Prospects for The Emergent Field of ns^2 Containing Solar Absorbers. *Chem. Commun.* **2017**, *53*, 20−44.

(20) Steinmann, V.; Brandt, R. E.; Buonassisi, T. Non-cubic solar cell materials. *Nat. Photonics* **2015**, *9*, 355.

(21) Tang, R.; Wang, X.; Jiang, C.; Li, S.; Liu, W.; Ju, H.; Yang, S.; Zhu, C.; Chen, T. n-Type Doping of Sb2S3 Light-Harvesting Films Enabling High-Efficiency Planar Heterojunction Solar Cells. *ACS Appl. Mater. Interfaces* **2018**, *10*, 30314−30321.

(22) Yuan, S.; Deng, H.; Dong, D.; Yang, X.; Qiao, K.; Hu, C.; Song, H.; Song, H.; He, Z.; Tang, J. Efficient Planar Antimony Sulfide Thin Film Photovoltaics with Large Grain and Preferential Growth. *Sol. Energy Mater. Sol. Cells* **2016**, *157*, 887−893.

(23) Kim, D.-H.; Lee, S.-J.; Park, M. S.; Kang, J.-K.; Heo, J. H.; Im, S. H.; Sung, S.-J. Highly Reproducible Planar Sb_2S_3-Sensitized Solar Cells Based on Atomic Layer Deposition. *Nanoscale* **2014**, *6*, 14549−14554.

(24) Osorio Mayon, Y.; White, T. P.; Wang, R.; Yang, Z.; Catchpole, K. R. Evaporated and Solution Deposited Planar Sb_2S_3 Solar Cells: A Comparison and its Significance. *Phys. Status Solidi A* **2016**, *213*, 108−113.

(25) Escorcia-García, J.; Becerra, D.; Nair, M. T. S.; Nair, P. K. Heterojunction CdS/Sb_2S_3 Solar Cells Using Antimony Sulfide Thin Films Prepared by Thermal Evaporation. *Thin Solid Films* **2014**, *569*, 28−34.

(26) Maiti, N.; Im, S. H.; Lim, C.-S.; Seok, S. I. A Chemical Precursor for Depositing Sb_2S_3 onto Mesoporous TiO_2 Layers in Non Aqueous Media and its Application to Solar Cells. *Dalton Trans.* **2012**, *41*, 11569−11572.

(27) Pawar, S. M.; Pawar, B. S.; Kim, J. H.; Joo, O.-S.; Lokhande, C. D. Recent Status of Chemical Bath Deposited Metal Chalcogenide and Metal Oxide Thin Films. *Curr. Appl. Phys.* **2011**, *11*, 117−161.

DOI: 10.1021/acsomega.9b01245
ACS Omega 2019, 4, 11380−11387

(28) Wang, G.; Wang, S.; Cui, Y.; Pan, D. A Novel and Versatile Strategy to Prepare Metal−Organic Molecular Precursor Solutions and its Application in Cu (In,Ga)(S,Se)$_2$ Solar Cells. *Chem. Mater.* **2012**, *24*, 3993−3997.
(29) Wang, X.; Li, J.; Liu, W.; Yang, S.; Zhu, C.; Chen, T. A Fast Chemical Approach Towards Sb2S3 Film with a Large Grain Size for High-Performance Planar Heterojunction Solar Cells. *Nanoscale* **2017**, *9*, 3386−3390.
(30) Hu, L.; Patterson, R. J.; Hu, Y.; Chen, W.; Zhang, Z.; Yuan, L.; Chen, Z.; Conibeer, G. J.; Wang, G.; Huang, S. High Performance PbS Colloidal Quantum Dot Solar Cells by Employing Solution-Processed CdS Thin Films from a Single-Source Precursor as the Electron Transport Layer. *Adv. Funct. Mater.* **2017**, *27*, 1703687−1703693.
(31) Žigas, L.; Audzijonis, A.; Grigas, J. Origin of Weak Ferroelectricity in Semiconductive Sb_2S_3 crystal. *J. Phys. Chem. Solids* **2017**, *101*, 5−9.
(32) Chen, X.; Li, Z.; Zhu, H.; Wang, Y.; Liang, B.; Chen, J.; Xu, Y.; Mai, Y. CdS/Sb_2S_3 Heterojunction Thin Film Solar Cells with a Thermally Evaporated Absorber. *J. Mater. Chem. C* **2017**, *5*, 9421−9428.
(33) DeAngelis, A. D.; Kemp, K. C.; Gaillard, N.; Kim, K. S. Antimony (III) Sulfide Thin Films as a Photoanode Material in Photocatalytic Water Splitting. *ACS Appl. Mater. Interfaces* **2016**, *8*, 8445−8451.
(34) Ouyang, B.; Meng, F.; Song, J. Energetics and Kinetics of Vacancies in Monolayer Graphene Boron Nitride Heterostructures. *2D Materials* **2014**, *1*, 035007.
(35) Williams, R. Surface Defects on Semiconductors. *Surfaces and Interfaces: Physics and Electronics*; Elsevier: 1983; pp 122−142.
(36) Lannoo, M. The Role of Dangling Bonds in the Properties of Surfaces and Interfaces of Semiconductors. *Rev. Phys. Appl.* **1990**, *25*, 887−894.
(37) Schmidt, J.; Merkle, A.; Brendel, R.; Hoex, B.; van de Sanden, M. C. M.; Kessels, W. M. M. Surface Passivation of High-Efficiency Silicon Solar Cells by Atomic-Layer-Deposited Al_2O_3. *Prog. Photovoltaics* **2008**, *16*, 461−466.
(38) Zhou, Y.; Wang, L.; Chen, S.; Qin, S.; Liu, X.; Chen, J.; Xue, D.-J.; Luo, M.; Cao, Y.; Cheng, Y. Thin-Film Sb_2Se_3 Photovoltaics with Oriented One-Dimensional Ribbons and Benign Grain Boundaries. *Nat. Photonics* **2015**, *9*, 409.
(39) Chang, P.; Cheng, H.; Li, W.; Zhuo, L.; He, L.; Yu, Y.; Zhao, F. Photocatalytic Reduction of o-Chloronitrobenzene Under Visible Light Irradiation Over CdS Quantum Dot Sensitized TiO_2. *Phys. Chem. Chem. Phys.* **2014**, *16*, 16606−16614.
(40) Van de Krol, R.; Liang, Y.; Schoonman, J. Solar Hydrogen Production with Nanostructured Metal Oxides. *J. Mater. Chem.* **2008**, *18*, 2311−2320.
(41) Jiang, C.; Xie, Y.; Lunt, R. R.; Hamann, T. W.; Zhang, P. Elucidating the Impact of Thin Film Texture on Charge Transport and Collection in Perovskite Solar Cells. *ACS Omega* **2018**, *3*, 3522−3529.
(42) Zakaznova-Herzog, V. P.; Harmer, S. L.; Nesbitt, H. W.; Bancroft, G. M.; Flemming, R.; Pratt, A. R. High Resolution XPS Study of the Large-Band-Gap Semiconductor Stibnite (Sb_2S_3): Structural Contributions and Surface Reconstruction. *Surf. Sci.* **2006**, *600*, 348−356.
(43) Silversmit, G.; Poelman, H.; Depla, D.; Barrett, N.; Marin, G. B.; De Gryse, R. A Comparative XPS and UPS Study of VOx Layers on Mineral TiO_2 (001)-Anatase Supports. *Surf. Interface Anal.* **2006**, *38*, 1257−1265.
(44) Han, Q.; Sun, S.; Sun, D.; Zhu, J.; Wang, X. Room-Temperature Synthesis from Molecular Precursors and Photocatalytic Activities of Ultralong Sb_2S_3 Nanowires. *RSC Adv.* **2011**, *1*, 1364−1369.
(45) Dhass, A.; Natarajan, E.; Ponnusamy, L. Influence of shunt resistance on the performance of solar photovoltaic cell. *Emerging Trends in Electrical Engineering and Energy Management (ICETEEEM), 2012 International Conference on, IEEE*, 2012; pp 382−386.
(46) El-Adawi, M. K.; Al-Nuaim, I. A. A Method to Determine the Solar Cell Series Resistance from a Single I−V. Characteristic Curve Considering its Shunt Resistance—New Approach. *Vacuum* **2001**, *64*, 33−36.
(47) Wolf, M.; Rauschenbach, H. Series Resistance Effects on Solar Cell Measurements. *Adv. Energy Convers.* **1963**, *3*, 455−479.
(48) Pai, N.; Lu, J.; Senevirathna, D. C.; Chesman, A. S. R.; Gengenbach, T.; Chatti, M.; Bach, U.; Andrews, P. C.; Spiccia, L.; Cheng, Y.-B. Spray Deposition of $AgBiS_2$ and Cu_3BiS_3 Thin Films for Photovoltaic Applications. *J. Mater. Chem. C* **2018**, *6*, 2483−2494.
(49) Suryawanshi, M. P.; Ghorpade, U. V.; Shin, S. W.; Pawar, S. A.; Kim, I. Y.; Hong, C. W.; Wu, M.; Patil, P. S.; Moholkar, A. V.; Kim, J. H. A Simple Aqueous Precursor Solution Processing of Earth-Abundant Cu_2SnS_3 Absorbers for Thin-Film Solar Cells. *ACS Appl. Mater. Interfaces* **2016**, *8*, 11603−11614.
(50) Li, D.-B.; Yin, X.; Grice, C. R.; Guan, L.; Song, Z.; Wang, C.; Chen, C.; Li, K.; Cimaroli, A. J.; Awni, R. A. Stable and Efficient CdS/Sb_2Se_3 Solar Cells Prepared by Scalable Close Space Sublimation. *Nano Energy* **2018**, *49*, 346−353.
(51) Zhang, W.; Saliba, M.; Moore, D. T.; Pathak, S. K.; Hörantner, M. T.; Stergiopoulos, T.; Stranks, S. D.; Eperon, G. E.; Alexander-Webber, J. A.; Abate, A. Ultrasmooth Organic−Inorganic Perovskite Thin-Film Formation and Crystallization For Efficient Planar Heterojunction Solar Cells. *Nat. Commun.* **2015**, *6*, 6142.
(52) Kovacik, P.; Assender, H. E.; Watt, A. A. R. Morphology Control in Co-Evaporated bulk Heterojunction Solar Cells. *Sol. Energy Mater. Sol. Cells* **2013**, *117*, 22−28.
(53) Qiao, S.; Liu, J.; Li, Z.; Wang, S.; Fu, G. Sb_2S_3 Thickness-Dependent Lateral Photovoltaic Effect and Time Response Observed in Glass/FTO/CdS/Sb_2S_3/Au Structure. *Opt. Express* **2017**, *25*, 19583−19594.
(54) Tashkandi, M.; Sampath, W. Morphology of CdS thin films: Pinholes and their effect on open circuit Voltage in CdS/CdTe solar cells. *Photovoltaic Specialists Conference (PVSC), 2011 37th IEEE*, 2011; pp 001700−001704.
(55) Kirchartz, T.; Agostinelli, T.; Campoy-Quiles, M.; Gong, W.; Nelson, J. Understanding the Thickness-Dependent Performance of Organic Bulk Heterojunction Solar Cells: The Influence of Mobility, Lifetime, and Space Charge. *J. Phys. Chem. C* **2012**, *3*, 3470−3475.
(56) Englman, T.; Terkieltaub, E.; Etgar, L. High Open Circuit Voltage in Sb_2S_3/Metal Oxide-Based Solar Cells. *J. Phys. Chem. C* **2015**, *119*, 12904−12909.

DOI: 10.1021/acsomega.9b01245
ACS Omega 2019, 4, 11380−11387